High Frequency TiO_2 Nanotube Adapted Microwave Waveguide Resonator for High Sensitivity Ultraviolet Detection

Benjamin D. Wiltshire[1], Mahnaz Alijani[1,2], Sevda Mohammadi[1], Arezoo Hosseini[1], Jan M. Macak[2,3], Mohammad H. Zarifi[1]*

[1] Okanagan MicroElectronics and Gigahertz Applications (OMEGA) Laboratory, School of Engineering, University of British Columbia, Canada V1V 1V7.

[2] Central European Institute of Technology, Brno University of Technology, Purkynova 123, Brno 61200, Czech Republic.

[3] Center of Materials and Nanotechnology, Faculty of Chemical Technology, University of Pardubice, Nam. Cs. Legii 565, 53002 Pardubice, Czech Republic.

KEYWORDS Co-planar waveguide resonator, split ring resonator, TiO_2 nanotube membrane, real-time microwave sensing, UV detection.

ABSTRACT: Ultraviolet (UV) sensors are a key component in growing applications such as water quality treatment and environmental monitoring, with considerable interest in their miniaturization and enhanced operation. This work presents a passive gold coplanar waveguide split ring resonator (SRR) integrated with anodic self-organized TiO_2 nanotube (TNT) membranes with a thickness of 20 µm to provide real-time UV detection. The resonator operated as a one-port device to capture the reflection coefficient (S_{11}) signal, with a center frequency of 16 GHz and a notch amplitude of -88 dB. It was experimentally analyzed for its UV sensing capability in the range of 36.5 µW/cm^2 to 463 µW/cm^2. The high frequency resonator was improved through design choices including the addition of a tapered input

transmission line, wire bonding for practical device design, and an interdigitated capacitive ring gap. The high frequency also helped mitigate noise due to water vapor or environmental contaminants. S_{11} amplitude variation was found through both experiment and modelling to follow a linear trend with UV illumination intensity. The resonator exhibited over 45±2 dB shift in resonant amplitude under the highest UV illumination conditions, with a sensitivity of 0.084 dB / μWcm^{-2} and the potential to sense UV intensity as low as 2.7 $\mu W/cm^2$. The presented device enabled a repeatable and accurate microwave response under UV illumination with very high sensitivity, entirely through the use of passive circuit elements.

1. INTRODUCTION:

Ultraviolet (UV) detectors play a significant role in a variety of applications ranging from space, pharmaceutical, health, food quality testing, ozone-layer monitoring, material characterization, and environmental monitoring.[1–4] The shift towards quantification of UV light has recently gained popularity due to the emerging application of high energy radiation in sensing and treatment methods.[5] The demand for robust and precise UV detection has pushed research activities towards a new generation of UV-based sensors that can provide operators with a highly sensitive, robust, and inexpensive platform. Cost and ecological footprint are important parameters for UV-sensors used to detect radiation in tropical regions for public health,[6] and the need for a real-time UV monitoring system with automated data acquisition is paramount for the prevention of degenerative changes in skin cells, fibrous tissue, and blood vessels.[7]

Planar microwave resonator sensors have gained considerable attention due to their potential for real-time, robust, and CMOS-compatible sensing over a wide range of applications such as health,[8] environmental,[9] and food monitoring.[10] These sensors operate based on interactions between non-ionizing electromagnetic fields with material molecules via their permittivity and electromagnetic loss.[11] Through field interactions, planar microwave resonator sensors are capable of contactless detecting the dielectric properties of materials in their close proximity, and are able to represent these properties as

electrical parameters as a resonant amplitude and a resonant frequency.[12,13] In particular, split ring resonators (SRRs) offer the benefits of resonant sensing on a low-cost platform with a locally concentrated electromagnetic field,[14] providing a significantly high signal to noise ratio at the operation frequency beneficial for monitoring, classification, and characterization of solid and liquid materials.[12,15]

In recent approaches, the potential of planar microwave resonator sensors has been demonstrated for gas and vapor detection.[16,17] Conventional planar microwave sensors use metal traces over gas-insensitive polymeric substrates, which have been further improved by incorporating sensitive interface materials, such as zeolites, ZnO, and conductive polymers such as polyaniline and PEDOT:PSS in the structure of planar microwave resonators to significantly enhance the sensitivity of these sensors.[18–20] Material incorporation in the planar microwave sensors has also demonstrated a notable enhancement in their sensitivity to UV light.[21]

Wide-bandgap semiconductors such as TiO_2, ZnO, and SnO_2 have demonstrated a strong sensitivity to UV light irradiation with customizable dimensions that can be targeted to different applications.[22–25] In a pioneering work, Zarifi *et al.*[26] have demonstrated a low-cost and robust integration of self-organized anodic TNT membranes with a wide bandgap (anatase phase, 3.2 eV) with SRRs, to detect UV light using a microwave sensor. The sensor operates based on the permittivity and conductivity variation in the TNT membrane due to the illuminating UV-light. The TNT membrane absorbed incident light, exciting charge carriers which induced a change in the membrane's dielectric properties; these changes were then monitored by measuring the transmission gain of the resonator.[27] In a subsequent study, they successfully demonstrated the application of UV excited TNT-integrated planar microwave resonator sensors in humidity, volatile organic compounds, and self-assembled monolayer detection.[28] A recent work by Wiltshire *et al.*[29] presented a unique application of UV-excited, TNT-integrated planar microwave resonator sensor for liquid mixture characterization. The sensor was capable of detecting and characterizing a liquid sample beyond the electric-field region solely based on the transmitted UV-light through the sample liquid. The sensor has demonstrated a maximum amplitude sensitivity of 2.9 dB

over a 0–100 % span of transmitted light through the liquid sample, where the liquid was 3 cm away from the UV light source and 3 cm above the microwave sensor.

To enhance the resolution of microwave sensors in detecting UV light, Zarifi *et al.*[30] introduced active microwave resonator sensors, which can improve the quality factor of the sensor in 2~3 orders of magnitude. This method has employed positive feedback system to compensate for the electromagnetic loss in the sensor's environment and consequently achieves an accurate detection of dielectric properties variation. The reported sensor based on active planar microwave sensor has achieved UV sensitivity down to 2 nW/cm^2 over a long exposure time. However, the high sensitivity and resolution of active devices requires more design complexity, power consumption, fabrication costs, and potential failure modes than a passive structure. Despite all these efforts, enhancing the sensitivity of the microwave based UV sensors to UV light intensity is an ongoing challenge and requires improvements from material and microwave device perspectives.[31]

This work investigates the first use of a high frequency microwave resonator with TNT membrane integration for UV sensing. TNT membranes were integrated into a gold SRR with a coplanar waveguide (CPW) structure, the resonator was connected to the readout circuitry through a stepped transmission line and wire bonding for analysis of their sensing properties. The overall behavior of the robust sensor and its potential in UV sensitive applications were evaluated with a focus on improvements in sensitive and accurate operation due to the high frequency design.

2. EXPERIMENTAL SECTION

2.1. TNT Membrane Fabrication. Titanium foils (0.89 mm thick, Fisher Scientific, 99.7% purity) were cleaned via ultra-sonication with isopropanol and DI water sequentially for 10 min each, then dried at room temperature.

Electrochemical anodization in an EG-based (Sigma Aldrich 99%) electrolyte, containing 4% DI water and 0.09 M ammonium fluoride (Sigma Aldrich, 98%) was used for the anodization of Ti foils, at a constant potential of 60 V for 3 h with a separation distance of 3 cm.

In order to increase the conductivity, TNTs were annealed at 350 °C for 4 h to promote anatase phase crystallization. The TNTs were then anodized again in an identical electrolyte at 30 V for 30 min to create a layer between the annealed nanotubes and the substrate which could be removed with 5 min of ultrasonication in methanol, detaching the nanotubes from the substrate as a TNT membrane.

2.2. Characterization of Materials. To investigate the morphology of the obtained TNT membranes, a field emission scanning electron microscope (SEM, Tescan Mira 3 XMU) was employed to image the TNT membranes. SEM images used secondary electron capture with a 20 kV working voltage and a working distance of 15 mm.

The structural evaluation of TNT membranes was based on X-ray diffraction (XRD) measured using a diffractometer (Rigaku Ultima IV). The diffractometer was set up in Bragg−Brentano geometry using Cu Kα radiation (λ = 1.54 Å). A Cu lamp was operated at a current of 44 mA and a voltage of 40 kV.

2.3. Resonator Design and Operation. To achieve improvements in the UV sensing capabilities of the SRR, the resonator was designed and simulated using *HFSS Ansys* software to operate with a resonant frequency in the microwave Ku band (12.5 – 18 GHz). The resonator input was a single port design and the reflected S_{11} spectra was measured through the same port. The resonator was connected with a stepped transmission line to improve impedance matching between the resonator and the signal source. Dimensions of the resonator and its stepped transmission line are shown in Fig. 1a-c. The high frequency response was selected to avoid effects of humidity or other vapors which are more prominent

below 10 GHz.[32,33] The resonant amplitude and frequency of the designed resonator (Fig. 1b) were measured in the simulation environment to be 15.9 GHz and -32 dB.

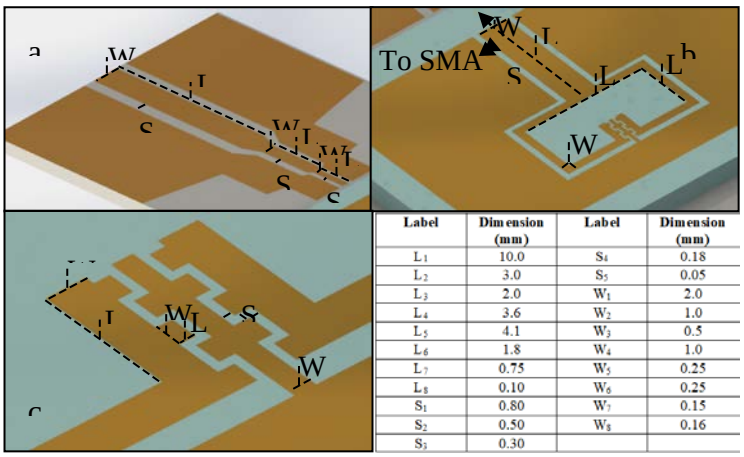

Label	Dimension (mm)	Label	Dimension (mm)
L_1	10.0	S_4	0.18
L_2	3.0	S_5	0.05
L_3	2.0	W_1	2.0
L_4	3.6	W_2	1.0
L_5	4.1	W_3	0.5
L_6	1.8	W_4	1.0
L_7	0.75	W_5	0.25
L_8	0.10	W_6	0.25
S_1	0.80	W_7	0.15
S_2	0.50	W_8	0.16
S_3	0.30		

Figure 1. Simulation model of the high frequency CPW resonator: **(a)** The stepped waveguide adapter, **(b)** the resonator design with **(c)** interdigitated capacitor for the high field region. Listed dimensions are included in the table bottom right.

To achieve the high frequency design the resonator was fabricated with sputtering and photolithographic processes on quartz as described in an earlier study.[34] A temperature-resistant quartz substrate was cleaned in an ultrasonication bath with acetone, water, and isopropanol for 10 min each. 10 nm of chromium for adhesion was sputtered below 100 nm of gold which was then patterned with photolithography and wet etch processing to fabricate a corrosion-resistant resonator pattern (Fig. 1a-d). The SRR was then wire bonded to a stepped CPW design fabricated on a 1 mm thick Rogers 6010 substrate with a permittivity of 10.2 and a loss tangent of 0.0023. The adapter was designed to minimize the effect of mismatch between the

SubMiniature A (SMA) connector and the resonator design, as such mismatch could cause unwanted reflections that prevent the signal from reaching the resonator, as seen from (1).

$$\frac{Z_L - Z_0}{Z_L + Z_0} = \Gamma \quad (1)$$

Here, Γ is the reflection coefficient and Z_L and Z_0 are the effective impedances of the load (the resonator) and source (the SMA and readout circuitry), respectively. Using transmission line and CPW theory, the effective impedance of the resonator input line shown in Fig. 1b can be found based on geometric properties.[35] However, a sharp change in impedance between the SMA and the ring design represents the maximum reflection coefficient and inefficient signal transfer to the resonator. Instead, the tapered design introduces a smoother impedance transition between the source and load, and beneficially allows for adjustment of the transmission line length, a key component of the overall impedance and signal reflection[36,37] as shown in (2).

$$Z_{(z)} = Z_0 \frac{Z_L + jZ_0 \tan(\beta z)}{Z_0 + jZ_L \tan(\beta z)} \quad (2)$$

Where *j* is the imaginary unit, βz is the electrical length of the tapered section, and Z_L and Z_0 are the effective impedance of the load and line. By iterating (2) from our resonator load along the tapered adapter to the 50 ohm SMA, a sequential method to track the impedance along the line is enabled without the need to implement more complex taper designs.[38]

Data was collected using the experimental setup shown in Fig. 2a,b. The experimental setup consisted of the resonator design connected to a vector network analyzer (VNA, Keysight N9552A). The interdigitated gap was identified through simulation as the region of highest electric field, indicating the highest sensitivity towards dielectric property variations. Therefore, during UV experiments, a TNT membrane was placed on the interdigitated gap to promote a highly sensitive response.

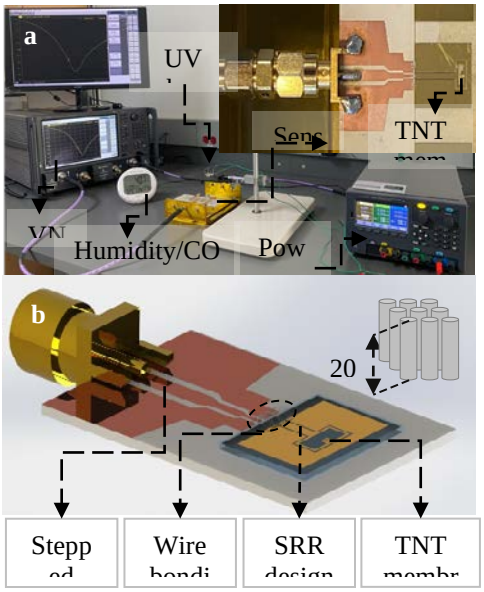

Figure 2. (a) Experimental setup used in UV sensing experiments with the fabricated resonator (inset) and **(b)** the resonator design highlighting the TNT membrane placement and the SMA to wire-bonding link used to adapt to the high frequency SRR design.

To analyze the UV sensing performance of the adapted CPW SRR, the resonator was connected to the VNA with an input signal power of -10 dBm, an intermediate frequency bandwidth of 300 Hz, and a frequency span of 4001 evenly spaced points between 15.8 GHz and 16.1 GHz. A variable-intensity UV LED was positioned 5 cm above the membrane and resonator and controlled by a power supply (Keysight E36200). LabVIEW software was used to capture and record the S_{11} spectra at 15 second intervals for the duration of the experiment.

3. RESULTS AND DISCUSSION

Self-organized anodic TNT membranes were prepared according to a previously well-established recipe and characterized to ensure conformation to the expected morphology and structure.[29] Fig. 3a presents the SEM images of the top view and cross-section of the TNT membranes with thickness of 20 μm and inner diameter of ~120 nm obtained from anodization at 60V for 6 h. Structure of the TNTs was analyzed prior to UV sensing to ensure adequate stability and responsivity. As-grown TNTs are amorphous and therefore significantly less conductive than crystalline TNTs which necessitates an annealing step[39]. Proper crystallinity is a key component in promoting strong UV absorption and affects the conductivity, mobility, and recombination of generated carriers in the material. The XRD pattern of the TNT membranes is shown in Fig. 3b. The diffraction patterns correspond to anatase TNT (JCPDS card number 21-1272) and hexagonal Ti from the substrate.

Figure 3. (a) SEM images of the top view and cross section (inset) of the TNT membrane, and **(b)** XRD pattern of TNT membranes obtained at 60 V for 6 h.

Characterization results reveal the vertical uniformity and expected dimensions of the grown TNT membranes. XRD results show that the TNT membrane were anatase, with titanium peaks from the underlying substrate also detected.

To begin analyzing the UV sensing performance of the CPW SRR, a baseline S_{11} spectrum of the reflected signal strength was measured using the blank (no TiO_2) resonator for comparison with the resonator after the TNT membranes were placed at the ring gap. With the TNT membrane vertically aligned and positioned above the ring gap, the UV LED illuminated the membrane with 365 nm wavelength (3.4 eV) UV light. To determine the sensitivity and accuracy of the resonator, varying currents were applied to the LED from 10 to 70 mA in steps of 10 mA at 30 min intervals. The S_{11} response measured by the VNA was recorded with LabVIEW software and converted into parameters of resonant amplitude and resonant frequency. After 5 min of illumination under different UV intensities, the S_{11} response was measured to analyze the behavior of the sensor and quantify its sensitivity, the collected spectra are shown in Fig. 4.

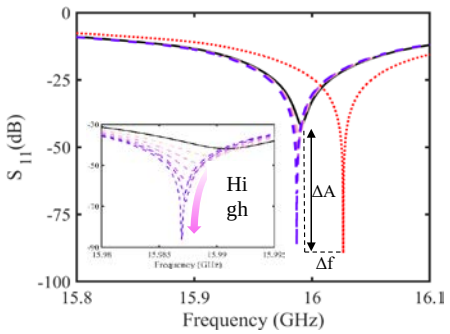

Figure 4. S_{11} profile of the sensor with TNT membranes (black) and the bare substrate (red, dotted) prior to UV illumination. Dashed lines represent the S_{11} spectrum after 5 min of illumination at different UV intensities (inset).

Initial results show that the bare high frequency sensor has a sharp resonant notch response at a frequency of 16.02 GHz with amplitude -88 dB (red, dotted). Positioning the TNT membranes above the ring gap introduced some loss and reduced the impedance matching, but the resonant response was still strongly matched and exhibited a resonant notch at 15.99 GHz and -41 dB (black). The significant shift in resonant amplitude when the TNTs were added, and the return to baseline when they are illuminated with UV light, indicated that the high frequency resonator design was extremely sensitive to variations in the TNT membranes permittivity.[26,30] The inset of Fig. 4 illustrates the effect of varying intensity UV light, as higher intensity UV exposure resulted in a larger amplitude and frequency shift in the recorded spectra due to increased charge carrier generation via the photoconductive effect.[40]

The LabVIEW software enabled the spectra in Fig. 4 to be recorded as resonant amplitudes and resonant frequencies over time, in order to quantify the sensitivity of the resonator and illustrate its accuracy. The results of the variable-power UV illumination are shown in Fig. 5(a), (b), and the collected results in resonant amplitude variation are further analyzed in Fig. 5(c).

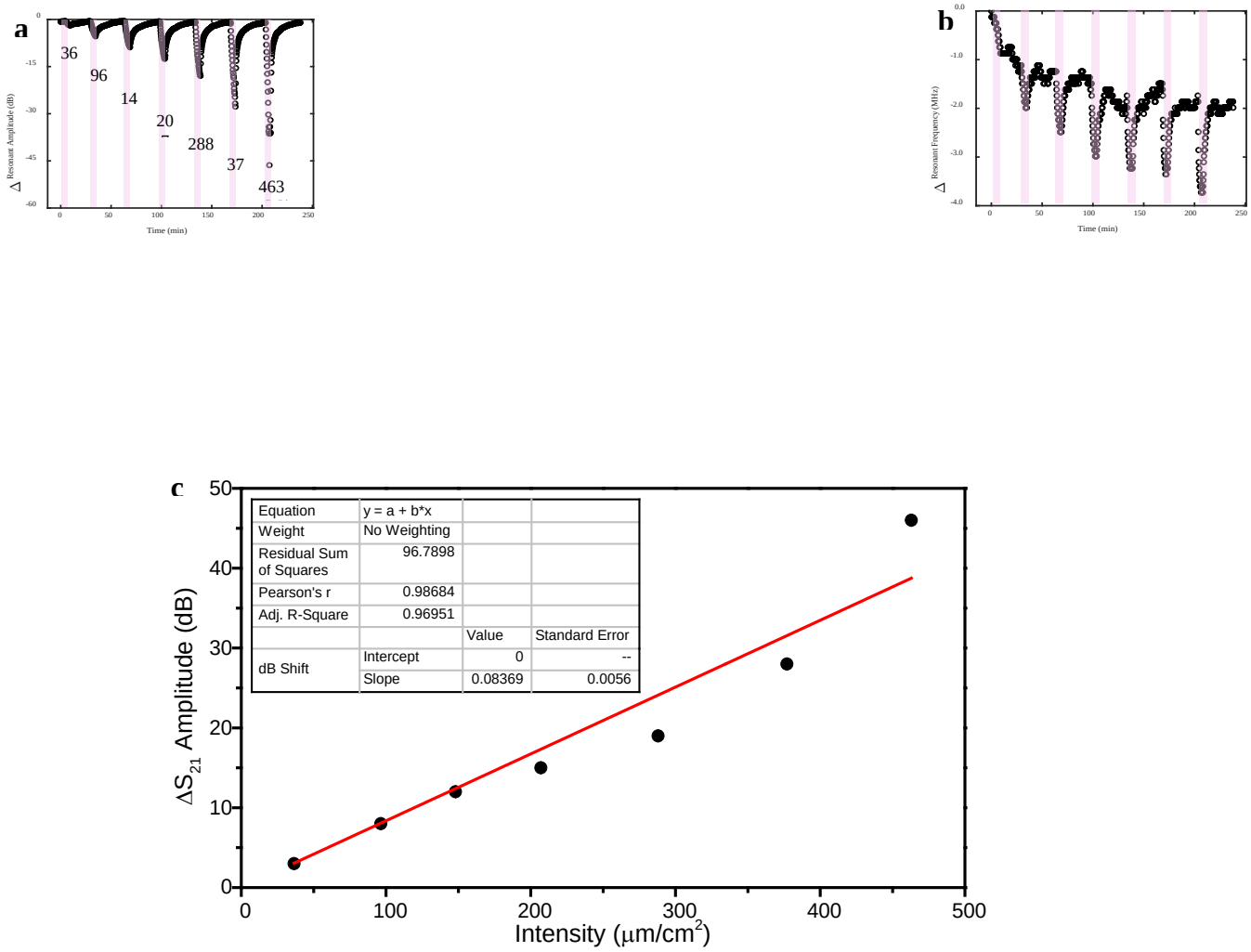

Figure 5. Experimental changes measured in **(a)** S_{11} resonant amplitude and **(b)** resonant frequency vs. time; **(c)** the resonant amplitude shift plotted against UV transmission for TNT membranes at different UV illumination from 36.5 to 463 μW/cm^2. The highlighted areas indicate UV exposure for 5 min.

Fig. 5 demonstrates the effectiveness of TNT integrated microwave resonators as UV sensors. Recording resonant amplitude (Fig. 5a) and resonant frequency (Fig. 5b) over time under periodic UV illumination showed that the resonant properties change monotonically with UV illumination from 36.5 to 463 μW/cm^2. Furthermore, Fig. 5a,b indicated that resonant amplitude was a more sensitive and quantifiable metric for accurate UV detection; with strong repeatability as the response returned to its baseline value within 30 min. The accuracy of amplitude variation

as a sensing measure could be ascribed to the strong absorption of UV rays by the large area of the TNT surface, which absorb the radiation at the surface of the nanotubes leading to large changes in surface conduction rather than the bulk permittivity, as shown in other studies.[26,41]

Sensitivity was found from the slope of Fig. 5c as 0.084 dB/μWcm^{-2}. The response at low UV intensities indicated that charge generation by the UV had a linear effect on the microwave impedance of the resonator which will be investigated later, whereas higher intensities might have introduced nonlinearities such as bulk defects, electron traps, or thermal noise. In this case, free charge carriers were generated by UV-induced electron excitation following the equation shown in (3).

$$TiO_2 + h\nu \rightarrow TiO_2^{+\bullet} + e \qquad (3)$$

Where hν represents the energy introduced by an incident UV photon of frequency, ν. This electrochemical reaction shows that upon illumination with UV light, crystalline TiO_2 can be excited into a reactive TiO_2 species ($TiO_2^{+\bullet}$) and a free electron (e^-). The rate of charge carrier generation and relaxation were not equal due to diffusion dynamics within the TNTs, holes will migrate to the surface and electrons move to the bulk, creating physical separation and slowing their recombination.[42,43] The recombination rate is also dependent on the carrier concentration based on band-to-band recombination (4.1), causing the response to begin saturating around 5 min of illumination for this length of nanotubes.

$$\frac{dn}{dt} = G - \frac{\Delta n}{\tau} \qquad (4.1)$$

Here dn/dt is the carrier concentration rate of change, G is the charge generation rate, Δn is the excess charge carrier concentration under UV illumination, and τ is the recombination time constant, a combination of non-radiative processes.[44] Experimentally, after sufficient time the

excess charge carrier concentration saturated because the recombination rate reached the generation rate. This equilibrium concentration, Δn_{eq}, is represented by (4.2)

$$\Delta n_{eq} = G\tau \qquad (4.2)$$

This equation showed a linear relationship between excess carrier concentration and carrier generation rate. Additional modelling was done in (5.1) to (5.7) to show that from impedance matching this resulted in a linear relationship between S_{11} variation and UV illumination for low intensity signals, supporting the accuracy of results from Fig. 5c.

To start, introducting free electrons in the TNTs could cause two major effects that contribute to UV detection with our microwave device. First, they could be easily polarized in an electric field, increasing the permittivity and capacitance of the membrane resulting in a reduction in resonant frequency. Second, they could contribute to electrical or polarization losses of the material. This increased loss reduced the resonant amplitude of the signal in the ring, and also strongly affected the matching of the resonator to the input transmission line based on (2) – a combinational effect that greatly reduced resonant amplitude.[26]

Mathematically, we can represent this effect by analyzing (1) as follows. At the resonant frequency, the bare device exhibited almost no reflection based on the deep resonant notch measured at -88 dB (5.1) which indicated that load and source impedance were effectively identical (5.2)

$$S_{11} = \left| \frac{Z_0 - Z_L}{Z_L + Z_0} \right| = 0 \qquad (5.1)$$

$$Z_0 = Z_L \qquad (5.2)$$

Here, the strong matching between the resonator and source simplified the expression by setting the real source and load impedance to be equal. Therefore, the only change in reflection

from the resonator loaded with TNTs was from the sample itself, which can be represented by an additional impedance Z_s included in (5.3)

$$S_{11,\,loaded} = \left| \frac{Z_0 - (Z_L + Z_s)}{Z_{L,loaded} + Z_0} \right| \cong \left| \frac{Z_s}{2Z_0} \right| \tag{5.3}$$

The impedance of the sample was found to be resistive based on the relatively large experimental change in resonant amplitude, as well as the wide bandgap of TiO_2 limiting conductivity of the sample, leading to (5.4)

$$Z_s = R_s = \frac{l}{A\sigma} = \frac{l}{A(\sigma_0 + \Delta\sigma)} \tag{5.4}$$

Where l and A are the effective length and area of current propagation in the TNT, σ_0 is the intrinsic conductivity of the TNT, and $\Delta\sigma$ is the conductivity change induced by excess generated charge carriers. Combining (5.3) and (5.4) and using the small signal condition that conductivity change is much less than intrinsic conductivity gives us an expression for S_{11} in terms of material parameters as shown below (5.5)

$$S_{11,\,loaded} = \frac{l}{2AZ_0(\sigma_0 + \Delta\sigma)} \cong \frac{R_s}{2Z_0\left(1 + \frac{\Delta\sigma}{\sigma_0}\right)} \tag{5.5}$$

This can be compared to experimental results by converting S_{11} to a dB scale (5.6)

$$S_{11,\,loaded} = log\left(\frac{R_s}{2Z_0}\right) - log\left(1 + \frac{\Delta\sigma}{\sigma_0}\right) \tag{5.6}$$

Further, for a small change in sample conductivity, particularly at low light intensities, we can rewrite the equation as a first order approximation (5.7)

$$S_{11,\,loaded} = log\left(\frac{R_s}{2Z_0}\right) - \frac{\Delta\sigma}{\sigma_0} = log\left(\frac{R_s}{2Z_0}\right) - \frac{q(\Delta n)\mu}{\sigma_0} \tag{5.7}$$

Therefore, for small UV intensities it was found from equations (4.2) and (5.7) that the device followed a linear relationship between S_{11} and the UV intensity, which supported low-intensity experimental results. The general reflection and scattering derivation (5.1-5.7) based on conductivity changes in materials can be applied to other sensing studies and are not limited to UV detection, and the authors have not seen a relationship between S_{11} and environmental sensing shown in this detail previously. (5.7) requires the condition that the conductivity change is much less than the intrinsic conductivity, which further explained why UV illumination did not follow the linear trend accurately at higher intensities.

With experimental results and modelling to support a linear relation between UV intensity and S_{11} amplitude variation, the relation between intensity and amplitude change at low UV intensities was used to calculate the minimum limit of detection (6).

$$LOD = \frac{3.33 \bullet SD}{b} = \frac{3.33 \bullet .07}{0.08369 \frac{dBcm^2}{\mu W}} = 2.7 \frac{\mu W}{cm^2} \qquad (6)$$

Here, *LOD* is the detection limit of interest, in this case, the smallest UV intensity measurable using this method. *SD* is the standard deviation of the low intensity sensing measurements (determined by analyzing the noise data of our low intensity UV measurements) and *b* is the amplitude sensitivity. The collected data showed that intensities down to 2.7 μW/cm^2 were detectable. These results represent an improvement over other passive UV microwave-based detection methods and are within an order of magnitude of active resonator devices under the same conditions.[26,30] Table 1 presents the amplitude responses fit to exponential curves to further analyze the overall shift and time constants of amplitude excitation and recovery.

Table 1. Summary of parameters extracted from S_{11} resonant frequency and resonant amplitude responses at different UV intensities.

UV ($\mu W/cm^2$)	ΔA (dB)	Δf (MHz)	τ_{exc} (s)	R^2_{exc}	τ_{rec} (s)	R^2_{rec}
36.5	-1.3	-0.99	-	-	1413.8	-
96.4	-4.8	-1.62	381.8	0.998	676.1	0.992
148	-8.3	-2.24	207.2	0.999	576.2	0.992
207	-11.6	-2.74	230.0	0.998	487.6	0.991
288	-16.9	-2.99	202.4	0.999	384.0	0.991
377	-26.8	-3.19	617.4	0.997	371.9	0.990
463	-45.3	-3.37	-	-	426.4	0.992

As can be seen in Table 1, the resonant amplitude variation was significantly higher than measured in previous studies and the result is completely monotonic with illumination intensity, moreover indicating accurate results. The excitation time and recovery time are in the range of seconds and minutes, indicating the presence of deep level traps or high energy defects, as shown previously with TNT-integrated microwave studies.[26,27,30] Further comparison for sensitivity and maximum parameter variation between UV sensing results of this study with other microwave resonators is shown below in Table 2.

Table 2. Comparison of important UV sensing parameters with other microwave resonator sensors.

Reference	Design	|ΔA| (dB)	Δf (MHz)	Sensitivity
[26]	5 GHz SRR	12.0	11.0	-
[28]	Surface-functionalized SRR	1.5	9.0	-
[30]	Active 8 GHz SRR	2.5	3.0	0.0016 dB/μWcm^{-2}
This study	High frequency 16 GHz SRR	45.3	2.0	0.084 dB/μWcm^{-2}

To further investigate the accuracy and repeatability of the sensor, the same experimental setup was used with a fixed current (70 mA, 463 $\mu W/cm^2$) applied to the UV light for 5 min intervals with 20 min intervals between UV illumination to allow for charge recombination. This UV

exposure was performed successively for 3 cycles to ensure repeatable results. This was the highest current setting used in this study; therefore, it was expected to represent the maximum variation in responses and the maximum possible degradation of the material or resonator under high intensity UV illumination over an extended time. S_{11} spectra were measured for these repeatability experiments and the change in resonant amplitude and resonant frequency over time were calculated and shown in Fig. 6.

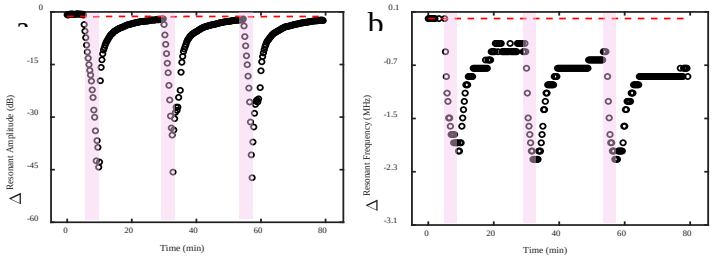

Figure 6. Experimental changes were measured in **(a)** S_{11} resonant amplitude and **(b)** resonant frequency vs. Time for TNT membranes under 463 μW/cm^2 UV illumination. The red dash lines present the bare substrate under 5 min UV illumination for 3 cycles. The purple highlighted areas represent UV illumination for 5 min.

Comparisons between Fig. 5 and 6 show that resonant amplitude can be used to measure UV illumination accurately and consistently and can quantify UV intensity based on its variation. Resonant frequency, primarily effected by changes in bulk permittivity of the TNT membrane, did not return to the baseline after 20 min, likely due to excited charges within the bulk taking longer to diffuse and recombine than those on the surface[41]. Resonant amplitude did not exhibit major variation in its maximum shift (44 to 47 dB) and no material or sensor breakdown under the UV light was apparent. The collected fitting parameters extracted from S_{11} resonant

frequency and amplitude are presented in Table 3, summarizing the results, and presenting the high frequency stepped-adapter design as a promising way forward for UV detection.

Table 3. Summary of parameters extracted from S_{11} resonant frequency and resonant amplitude responses at repeated 463 μW/cm^2 UV-illumination.

Cycle	**ΔA (dB)**	**Δf (MHz)**	**τ_{rec}**	**R^2_{rec}**
1st	-44.284	-3.6241	88.63	0.982
2nd	-45.696	-3.2492	127.92	0.986
3rd	-47.292	-2.9992	130.38	0.984

4. CONCLUSION

In summary, the design, simulation, and analysis of a high frequency, TNT-integrated SRR for UV sensing was performed. The resonant frequency was 16 GHz to decrease the effect of noise-inducing contaminants, primarily water vapor, around the TNT-integrated resonator. To achieve this high frequency, nanofabrication and a tapered transmission line were used in the design. The changing S_{11} resonant amplitude and frequency was measured while the anatase TNT membranes were illuminated with different UV intensities. Sensitivity of the resonator was found to be 0.084 dB/μWcm^{-2} with a maximum amplitude shift of ~45 dB and a LOD of 2.7 μWcm^{-2}. The resonator exhibited a repeatable and accurate response under UV light, returning to the baseline response after 20 min of sample relaxation in multiple controlled experiments. SRR performance was further analyzed by fitting the response to determine speed and magnitude of the shift. The presented improvements in these metrics combined with the accuracy and repeatability of the microwave-based UV sensor encourages further exploration in its use as an inexpensive and robust option in medical, environmental, and process monitoring.

AUTHOR INFORMATION

Corresponding Author

* E-mail address: mohammad.zarifi@ubc.ca (M.H. Zarifi).

ACKNOWLEDGMENT

The authors acknowledge the Syilx Okanagan Nation for use of their unceded territory, the land on which the research was conducted. We acknowledge support from the Natural Sciences and Engineering Research Council of Canada (NSERC), through grant RGPIN-2018-04288. We thank The Mathematics of Information Technology and Complex Systems (Mitacs) Accelerate program through grant no. IT19272, IT12995 and IT16696. The authors thank the Canadian Foundation for Innovation (CFI) through grants no.38148 as well as CMC microelectronics for their software licenses. M.A. would like to thank Youth and Sports of the Czech Republic (MEYS CR, LM2018103, CZ.02.1.01/0.0/0.0/17_048/0007421) and junior grant project 2021–2022 (CEITEC VUT-J-21-7397) of Brno University of Technology. B.D.W. would like to thank NSERC CGS D scholarship support (No. 535553).

REFRENCES

(1) Ding, W.; Meng, X. High Performance Solar-Blind UV Detector Based on β-Ga_2O_3/GaN Nanowires Heterojunction. *J. Alloys Compd.* **2021**, *866*, 157564.

(2) Brown, B.; Ward, A.; Fazili, Z.; Østergaard, J.; Asare-Addo, K. Application of UV Dissolution Imaging to Pharmaceutical Systems. *Adv. Drug Deliv. Rev.* **2021**, *177*, 113949.

(3) Carotta, M. C.; Cervi, A.; Fioravanti, A.; Gherardi, S.; Giberti, A.; Vendemiati, B.; Vincenzi, D.; Sacerdoti, M. A Novel Ozone Detection at Room Temperature through UV-LED-Assisted ZnO Thick Film Sensors. *Thin Solid Films* **2011**, *520* (3), 939–946.

(4) Razeghi, M.; Rogalski, A. Semiconductor Ultraviolet Detectors. *J. Appl. Phys.* **1996**, *79*

(10), 7433–7473.

(5) Bourgeois, W.; Burgess, J. E.; Stuetz, R. M. On-Line Monitoring of Wastewater Quality: A Review . *Journal of Chemical Technology & Biotechnology* . John Wiley & Sons, Ltd : Chichester, UK **2001**, pp 337–348.

(6) Kerr, J. B.; Fioletov, V. E. Surface Ultraviolet Radiation. *Atmosphere-Ocean* **2008**, *46* (1), 159–184.

(7) Huang, X.; Chalmers, A. N. Review of Wearable and Portable Sensors for Monitoring Personal Solar UV Exposure. *Ann. Biomed. Eng.* **2021**, *49* (3), 964–978.

(8) Camli, B.; Kusakci, E.; Lafci, B.; Salman, S.; Torun, H.; Yalcinkaya, A. A Microwave Ring Resonator Based Glucose Sensor. *Procedia Eng.* **2016**, *168*, 465–468.

(9) Mohammadi, S.; Nadaraja, A. V.; Roberts, D. J.; Zarifi, M. H. Real-Time and Hazard-Free Water Quality Monitoring Based on Microwave Planar Resonator Sensor. *Sensors Actuators A Phys.* **2020**, *303*, 111663.

(10) Tanguy, N. R.; Fiddes, L. K.; Yan, N. Enhanced Radio Frequency Biosensor for Food Quality Detection Using Functionalized Carbon Nanofillers. *ACS Appl. Mater. Interfaces* **2015**, *7* (22), 11939–11947.

(11) Martín, F.; Vélez, P.; Gil, M. Microwave Sensors Based on Resonant Elements. Multidisciplinary Digital Publishing Institute 2020.

(12) Velez, P.; Su, L.; Grenier, K.; Mata-Contreras, J.; Dubuc, D.; Martin, F. Microwave Microfluidic Sensor Based on a Microstrip Splitter/Combiner Configuration and Split Ring Resonators (SRRs) for Dielectric Characterization of Liquids. *IEEE Sens. J.* **2017**, *17* (20), 6589–6598.

(13) Ebrahimi, A.; Withayachumnankul, W.; Al-Sarawi, S.; Aboott, D. High-Sensitivity Metamaterial-Inspired Sensor. *IEEE Sens. J* **2014**, *14* (14(5)), 1345–1351.

(14) Muñoz-Enano, J.; Vélez, P.; Gil, M.; Martín, F. Planar Microwave Resonant Sensors: A Review and Recent Developments. *Applied Sciences* . **2020**.

(15) Jha, A. K.; Akhter, Z.; Tiwari, N.; Shafi, K. T. M.; Samant, H.; Akhtar, M. J.; Cifra, M. Broadband Wireless Sensing System for Non-Invasive Testing of Biological Samples. *IEEE J. Emerg. Sel. Top. Circuits Syst.* **2018**, *8* (2), 251–259.

(16) Korostynska, O.; Mason, A.; Al-Shamma'A, A. Microwave Sensors for the Non-Invasive Monitoring of Industrial and Medical Applications. *Sens. Rev.* **2014**.

(17) Rydosz, A.; Maciak, E.; Wincza, K.; Gruszczynski, S. Microwave-Based Sensors with Phthalocyanine Films for Acetone, Ethanol and Methanol Detection. *Sensors Actuators B Chem.* **2016**, *237*, 876–886.

(18) Tanguy, N. R.; Wiltshire, B.; Arjmand, M.; Zarifi, M. H.; Yan, N. Highly Sensitive and Contactless Ammonia Detection Based on Nanocomposites of Phosphate-Functionalized Reduced Graphene Oxide/Polyaniline Immobilized on Microstrip Resonators. *ACS Appl. Mater. Interfaces* **2020**, *12* (8), 9746–9754.

(19) Moradpour, M.; Hosseini, E.; Jain, M. C.; Narang, R.; Tanguy, N.; Zarifi, M. H. Patterned PEDOT:PSS-Enabled Organic Planar Microwave Resonator Sensors. *Appl. Mater. Today* **2021**, *24*, 101106.

(20) Dietrich, M.; Rauch, D.; Simon, U.; Porch, A.; Moos, R. Ammonia Storage Studies on H-ZSM-5 Zeolites by Microwave Cavity Perturbation: Correlation of Dielectric Properties with Ammonia Storage. *J. Sensors Sens. Syst.* **2015**, *4* (2), 263–269.

(21) Benlamri, M.; Deif, S.; Mahdi, N.; Baghelani, M.; Zarifi, M. H.; Barlage, D. W.; Shankar, K.; Daneshmand, M. Planar Microwave Resonator with Electrodeposited ZnO Thin Film for Ultraviolet Detection. *Semicond. Sci. Technol.* **2019**, *35* (2), 25003.

(22) Ng, S.; Kuberský, P.; Krbal, M.; Prikryl, J.; Gärtnerová, V.; Moravcová, D.; Sopha, H.; Zazpe, R.; Yam, F. K.; Jäger, A.; et al. ZnO Coated Anodic 1D TiO_2 Nanotube Layers: Efficient Photo-Electrochemical and Gas Sensing Heterojunction. *Adv. Eng. Mater.* **2018**, *20* (2), 1700589.

(23) Ng, S.; Kubersky, P.; Krbal, M.; Prikryl, J.; Gärtnerov, V.; Moravcov, D.; Sopha, H.; Zazpe, R.; Yam, F. K.; Macak, J. M. ZnO Coated Anodic 1D TiO_2 Nanotube Layers : Efficient Photo-Electrochemical and Gas Sensing Heterojunction A. **2017**, *1700589*, 1–10.

(24) Pereira, J. R.; Zazpe, R.; Ng, S.; Pra, J.; Pr, J.; Krbal, M.; Sopha, H.; Maca, J. M.; Michalic, J. Atomic Layer Deposition of SnO_2 - Coated Anodic One-Dimensional TiO_2 Nanotube Layers for Low Concentration NO_2 Sensing. **2020**, No. 2.

(25) Alijani, M.; Sopha, H.; Ng, S.; Macak, J. M. High Aspect Ratio TiO_2 Nanotube Layers Obtained in a Very Short Anodization Time. *Electrochim. Acta* **2021**, 138080.

(26) Zarifi, M. H.; Mohammadpour, A.; Farsinezhad, S.; Wiltshire, B. D.; Nosrati, M.; Askar, A. M.; Daneshmand, M.; Shankar, K. Time-Resolved Microwave Photoconductivity (TRMC) Using Planar Microwave Resonators: Application to the Study of Long-Lived

Charge Pairs in Photoexcited Titania Nanotube Arrays. *J. Phys. Chem. C* **2015**, 150615093503007.

(27) Zarifi, M. H.; Wiltshire, B. D.; Mahdi, N.; Shankar, K.; Daneshmand, M. Distinguishing between Deep Trapping Transients of Electrons and Holes in TiO_2 Nanotube Arrays Using Planar Microwave Resonator Sensor. *ACS Appl. Mater. Interfaces* **2018**, *10* (35), 29857–29865.

(28) Zarifi, M. H.; Farsinezhad, S.; Wiltshire, B. D.; Abdorrazaghi, M.; Mahdi, N.; Kar, P.; Daneshmand, M.; Shankar, K. Effect of Phosphonate Monolayer Adsorbate on the Microwave Photoresponse of TiO_2 Nanotube Membranes Mounted on a Planar Double Ring Resonator. *Nanotechnology* **2016**, *27* (37).

(29) Wiltshire, B. D.; Zarifi, M. H. TiO_2 Nanotube-Integrated Microwave Planar Resonator Sensor for Ultraviolet Transmission-Based Liquid Characterization. *Sensors Actuators B Chem.* **2021**, *341*, 130014.

(30) Zarifi, M. H.; Wiltshire, B.; Mahdi, N.; Kar, P.; Shankar, K.; Daneshmand, M. Ultraviolet Sensing Using a TiO_2 Nanotube Integrated High Resolution Planar Microwave Resonator Device. *Nanoscale* **2018**, *10* (10).

(31) Su, L.; Mata-Contreras, J.; Vélez, P.; Martín, F. A Review of Sensing Strategies for Microwave Sensors Based on Metamaterial-Inspired Resonators: Dielectric Characterization, Displacement, and Angular Velocity Measurements for Health Diagnosis, Telecommunication, and Space Applications. *Int. J. Antennas Propag.* **2017**, *2017*, 1–13.

(32) Borgese, M.; Dicandia, F. A.; Costa, F.; Genovesi, S.; Manara, G. An Inkjet Printed Chipless RFID Sensor for Wireless Humidity Monitoring. *IEEE Sens. J.* **2017**, *17* (15), 4699–4707.

(33) Park, J.-K.; Kang, T.-G.; Kim, B.-H.; Lee, H.-J.; Choi, H. H.; Yook, J.-G. Real-Time Humidity Sensor Based on Microwave Resonator Coupled with PEDOT:PSS Conducting Polymer Film. *Sci. Rep.* **2018**, *8* (1), 439.

(34) Mohammadi, S.; Wiltshire, B.; Jain, M. C.; Nadaraja, A. V; Clements, A.; Golovin, K.; Roberts, D. J.; Johnson, T.; Foulds, I.; Zarifi, M. H. Gold Coplanar Waveguide Resonator Integrated with a Microfluidic Channel for Aqueous Dielectric Detection. *IEEE Sens. J.* **2020**, 1.

(35) Simons, R. Coplanar Waveguide Circuits, Components, and Systems . John Wiley : New York .

(36) Rupali; Rajni, R. A Review of Stepped Impedance Resonators in Microwave Circuits. *Int. J. Comput. Sci. Netw.* **2017**, 54–60.

(37) Nataraj, B.; Prabha, K. R. Analysis and Modeling of Various Tapered Coplanar Waveguide . *IOP conference series. Materials Science and Engineering* . IOP Publishing : Bristol **2021**, p 12044.

(38) Lee, K.-A.; Ko, K.-C. Modeling of Electromagnetic Wave Propagation with Tapered Transmission Line . *Jpn J Appl Phys* . The Japan Society of Applied Physics 2012, pp 09MG01-09MG01-3.

(39) Das, S.; Zazpe, R.; Prikryl, J.; Knotek, P.; Krbal, M.; Sopha, H.; Podzemna, V.; Macak, J. M. Influence of Annealing Temperatures on the Properties of Low Aspect-Ratio TiO2 Nanotube Layers. *Electrochim. Acta* **2016**, *213*, 452–459.

(40) Schindler, K. M.; Kunst, M. Charge-Carrier Dynamics in Titania Powders. *J. Phys. Chem.* **1990**, *94* (21), 8222–8226.

(41) Zhang, L.; Mohamed, H. H.; Dillert, R.; Bahnemann, D. Kinetics and Mechanisms of Charge Transfer Processes in Photocatalytic Systems: A Review. *J. Photochem. Photobiol. C Photochem. Rev.* **2012**, *13* (4), 263–276.

(42) Mor, G. K.; Varghese, O. K.; Paulose, M.; Shankar, K.; Grimes, C. A. A Review on Highly Ordered, Vertically Oriented TiO2 Nanotube Arrays: Fabrication, Material Properties, and Solar Energy Applications. *Sol. Energy Mater. Sol. Cells* **2006**, *90* (14), 2011–2075.

(43) Zhou, X.; Liu, N.; Schmuki, P. Photocatalysis with TiO_2 Nanotubes: “Colorful” Reactivity and Designing Site-Specific Photocatalytic Centers into TiO2 Nanotubes. *ACS Catal.* **2017**, *7* (5), 3210–3235.

(44) Wang, X.; Feng, Z.; Shi, J.; Jia, G.; Shen, S.; Zhou, J.; Li, C. Trap States and Carrier Dynamics of TiO_2 Studied by Photoluminescence Spectroscopy under Weak Excitation Condition. *Phys. Chem. Chem. Phys.* **2010**, *12* (26), 7083–7090.

GRAPHICAL ABSTRACT